Solidification cracking during welding of steel: In situ X-ray observation

IOP Conf. Series: Materials Science and Engineering **529** (2019) 012026 doi:10.1088/1757-899X/529/1/012026

Solidification cracking during welding of steel: *In situ* X-ray observation

L. Aucott[a], J. Li[a], A. Rack[b], H. B. Dong[a] *
[a] Department of Engineering, University of Leicester, UK
[b] European Synchrotron Radiation Facility, Grenoble, France
Corresponding author: hd38@le.ac.uk

Abstract. Solidification cracking is an important issue during welding, casting and some of the additive manufacturing process. In order to illuminate the failure mechanisms, solidification cracking during arc welding of steel are investigated in situ with high-speed, high energy, synchrotron X-ray radiography approach. Analysis of the *in situ* radiography sequence revealed the solidification cracking initiates in the weld sub-surface trailing the welding electrode at relatively low true strain of about 3.1% in the form of micro-cavities. Although both material type and bending speed influence solidification cracking, cracks propagate from the core of the weld towards the free surface along the solidifying grain boundaries was found at a speed of between 1.7 -2.6 × 10^{-3} m s^{-1} for three different steels. In addition, a three-stage mechanistic model for solidification cracking during welding of steel is proposed.

1. Introduction

Solidification cracking, also known as hot cracking, is a key phenomenon associated with fusion welding, casting and some of the additive manufacturing processes. If undetected, the cracking defects can act as stress concentration sites which lead to premature failure via fatigue, as well as offer favourable sites for hydrogen assisted cracking [1, 2] and stress corrosion cracking [3]. Therefore, the solidification cracking is widely studied and have been the subject of investigation for several decades [4-6].

Early experimental efforts to observe the phenomenon were focussed on favourable organic alloys because of the technical problems involved with metallic alloys. Farup *et al* [7] successfully observed solidification cracking *in situ* in a directionally solidified succinonitrile-acetone alloy using a Bridgman type experiment under a microscope. Recent *in situ* observations of semi-solid deformation and solidification cracking in metallic alloys has been born from the interesting new fields of experimental research created by the development of third generation synchrotron sources. Gourlay *et al* [8] demonstrated the existence and importance of granular behaviour in solidification using *in situ* radiography experiments. Vernede, Rappaz, and co-workers then adopted the granular simulation method for discrete element simulations of solidification cracking [9-11]. The studies show that solidification cracking is a highly complex phenomenon, which involves heat flow, fluid flow under capillary action and various other factors such as material chemistry and processing parameters. Phillion *et al* [12] used a synchrotron micro-tomography approach to image the three dimensional morphology of solidification cracks in aluminium alloy AA5182. A similar approach was then employed by Aveson *et al* [13], although at a much smaller scale, to observe the initiation and propagation of solidification cracks at the dendritic scale in an Al-Sn binary alloy. Kareh *et al* [14] utilised time-resolved tomography to reveal that grains in semi-solid equiaxed Al-Cu alloys deform and rotate as independent bodies under compressive load.

In this research, a novel small-scale Varestraint test rig (ADW test rig) has been developed and embedded into the European Synchrotron Radiation Facilities (ESRF) high resolution imaging beamline, ID19. The beamline is installed on a low-beta section of the storage ring. ID19 has a small source size (30 µm vertical x 120 µm horizontal) and long 145 m straight section from the source to experimental hutch. This allows for the coherence properties of the beam to be exploited [15]. Solidification cracking during welding of steel is observed *in situ* using high-speed, high-energy radiography.

2. Materials and methodology

Figure 1 shows the experimental setup and schematic illustration of the test apparatus components. The equipment is designed to carry out stand-alone small-scale Varestraint weldability tests, while also allowing for integration to ESRF ID19 experimental hutch. The welding was carried out using a tungsten inert gas (TIG) weld method at 10 V and 98-108 A with a non-consumable tungsten electrode in DC-ve polarity.

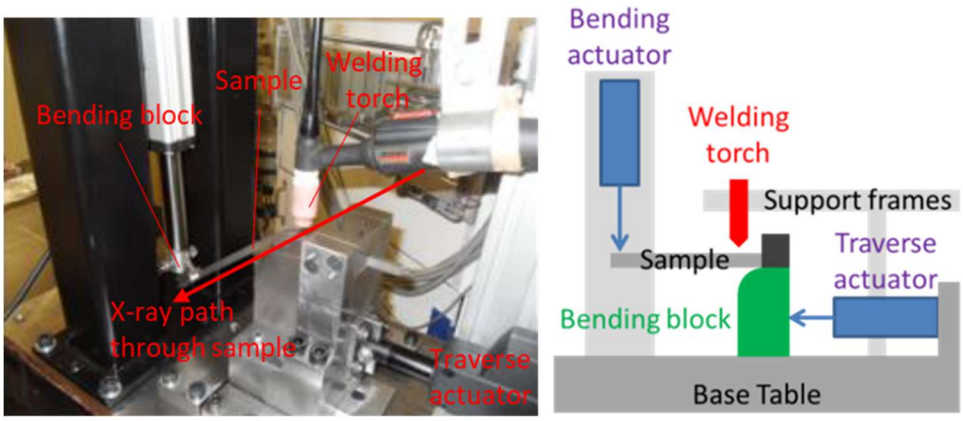

Figure 1: a) Varestraint test rig embedded into ID19, b) Schematic illustration of the test apparatus components.

8 mm square samples were created 300 mm long from three steels with poor weldabilty. The chemistry of the materials is defined in Table 1. To improve X-ray image quality, it is imperative to obtain the smallest path length through the sample. The 8 mm sample thickness was selected as it was the smallest feasible to weld upon. The samples were locked into the clamping device on top of the bending radius with a 30 mm overhang to attach the earth clamp for welding.

Table 1: Nominal chemistries of sample materials.

	C	Mn	Si	P	S	Cr	Ni
Mild Steel-EN1A	0.15	1	0.35	0.06	0.6	--	--
Stainless Steel-S303	0.15	2	1	0.2	0.15	19	10
Carbon Steel	0.4	0.9	0.2	0.06	0.6	--	--

The bending block assembly (with the sample clamped in) is attached to one of two electric actuators powered by a 12 V battery. The horizontally orientated actuator in Figure 1 supplies a load at speeds of up to 14 mm/s across a 40 mm stroke length. This actuator is connected to the bending block assembly and traverses it along the table to create the motion to weld a 40 mm length along the sample. Guide rails located on the surface of the base table interlink with the bending block assembly to ensure a straight travel path, normal to the beam. The opposite side of the test sample is then attached to a second actuator with a vertical orientation. This provides a load at speeds of up to 135 mm/s across a 150 mm stroke length. This actuator bends the sample during welding. The bending causes the sample to deform around the radius (60 mm) of the bending block and induces an augmented strain to the sample to

stimulate solidification cracking. The weld pool solidification temperature was measured by tungsten-rhenium Type C thermocouples.

In order to reach a sufficiently high photon flux density at the desired X-ray energy of around 110 keV, ID19 was operated in white beam mode. The light of the beamline's wiggler (gap 45) was filtered by a diamond window, 5.6 mm Al and 6 mm Cu. The resulting bandwidth is comparably large (delta_E/E = 90%, peak around 117 keV) but allows for radiography imaging at frame rates up to 1 kHz. The resultant photon flux density was approximately 7 x 10^{11} photons $mm^{-1}s^{-1}$. For the imaging, a view window of 1872 x 1000 pixels was employed with a 10 μm/pixel resolution. The camera recorded continuously images at a rate of 1000 fps to satisfy the temporal demands in observing the solidification cracking *in situ*. All post-processing was performed with freely available ImageJ software. A simple processing routine was implemented for all analysis.

3.Results and discussion

3.1Solidification cracks at macro-scale

The novel small-scale Varestraint test rig commissioned for the tests successfully produces

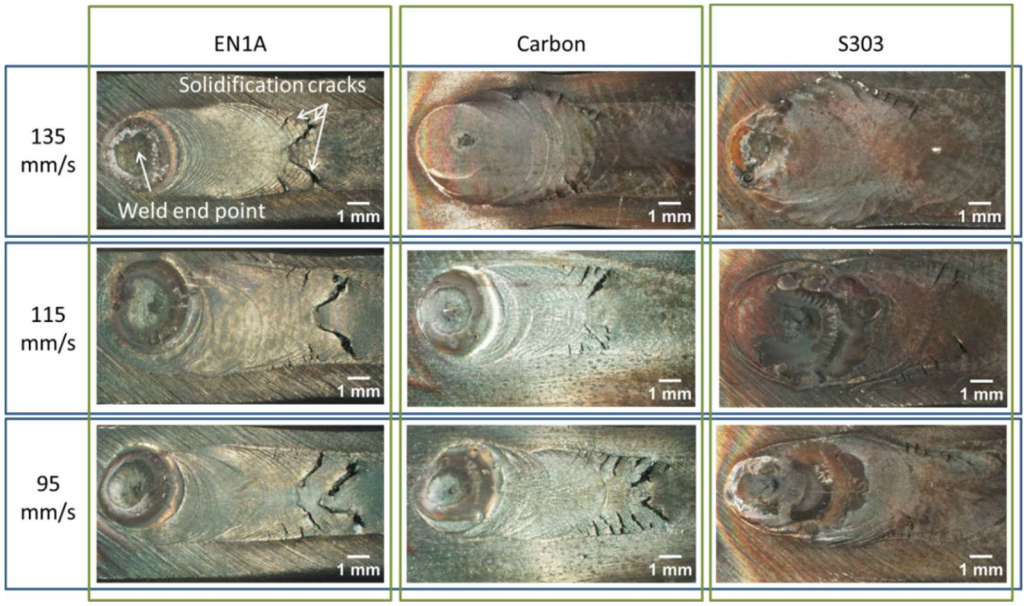

Figure 2: The array of weld solidification cracking observed in EN1A, Carbon, and S303 materials tested at 135, 115, and 95 mm/s bending speeds.

consistent and repeatable solidification cracks. Figure 2 displays macro images of the surface cracking observed in the samples selected for analysis. Each of the nine tests depicted in Figure 2 was repeated three times to ensure that the results obtained were consistent. It is evident from initial inspection of Figure 2 that both the material type and bending speed employed during Varestraint testing has significant impact on solidification cracking.

ImageJ software was used to quantify the surface cracking observed in the samples in terms of total crack length criterion (TCL) with the results plotted in Figure 3. TCL is derived from:

$$TCL = \Sigma Crack1 + Crack2 + \cdots CrackN \quad (1)$$

Analysis of Figure 3 confirms that both material type and bending speed influence solidification cracking. There is clearly a 3 tier susceptibility based on material type, with the EN1A sample being the most susceptible, and the S303 being the least susceptible. It is also evident from Figure 3 that the TCL

of solidification cracks is also heavily dependent upon the bending speed utilised during Varestraint testing.

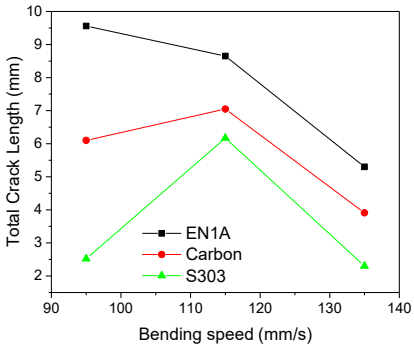

Figure 3: Total length of surface solidification cracking observed in the weld after Varestraint testing at a range of bending speeds.

3.2 In situ radiography imaging of solidification cracking in welding

Figure 4 displays the selected initiation and end stages of the cracking from the processed radiographs. The white tip in the top left of the images is the tungsten welding electrode. The large white part in the centre of the images is an EN1A test sample. Figure 4a) highlights the point at which weld solidification cracks were observed to initiate in the radiography sequence. The cracks are easily distinguishable, being darker than the bulk sample. This is due in part to a lower attenuation through the cracking interface. However, the main source of the interface clarity can be attributed to the refraction based coherent imaging technique and wide propagation distance between the sample and detector.

The cracks appear after 0.134 s of bending under a loading rate of 135 mm/s. The approximate strain at cracking initiation is 3.25%. The solidification cracks appear to initiate trailing the welding electrode by 2.69 mm at 1.45 mm sub-surface. The velocity of the fracture is measured at approximately 2.2 mm/s in the 2D plane of imaging, which could equate to speeds of up to 3.2mm/s to the 3D nature of the cracking when considering propagation at angles up to 45° in the z plane.

After the initial cracks have penetrated the surface, further cracking then begins to initiate sub-surface in the region to the left of the initial nucleation site (closer to the heat source) and follow the same vertical propagation path. This time however, it appears that the cracks also begin to converge laterally with the initial crack. Cracking continues to develop in this manner until 0.832s of bending (Figure *4*4b). The cracks then cease to develop at 10.53% strain. From the analysis it is possible to conclude that the weld solidification cracking occurred in the EN1A sample (with a 135 mm/s bending rate) over a 3.25-10.53% strain range and 0.698s time period.

The same analysis was completed for all samples referenced in Figure 2. The results are presented in Table 2. All solidification cracks were found to initiate sub-surface during analysis of micro-radiographs. It is clear that the least susceptible material – the S303 alloy – initiates at a shallower (0.47 – 0.98 mm) location when compared to the more susceptible EN1A and Carbon alloys. Furthermore, it also demonstrates that solidification cracks initiate at lower strains (2.42 – 3.42 %) in the more susceptible materials - the EN1A and carbon alloys. In the less susceptible S303 alloy, the cracks do not appear until strains have reached 4.00 – 5.06 %. The most susceptible material in terms of the commonly applied TCL criterion – the EN1A sample – exhibits the widest strain range in which solidification cracking propagates. The least susceptible alloy – the S303 sample – exhibits the shortest strain range. Again, it is apparent that all of the features are again heavily dependent upon the Varestraint bending speed. However, the measured fracture velocity remains fairly consistent throughout the experiments with an average velocity of 2.33 mm/s calculated.

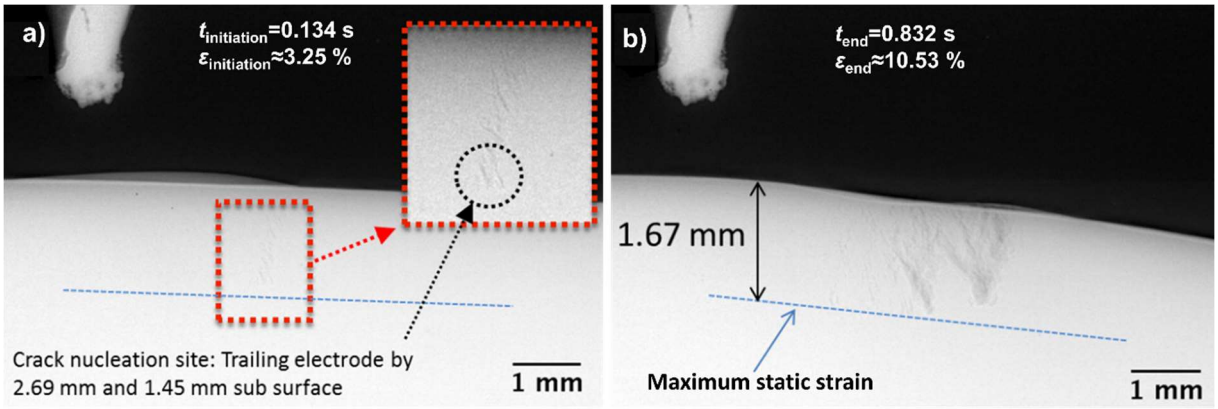

Figure 4: Results of synchrotron radiography analysis on the EN1A sample tested with a 135 mm bending speed, showing a) the initiation of weld solidification cracking at 0.134s of bending with an approximate strain of 3.25 %, the broken blue line depicts the fusion boundary measured from post-test microscopic observations b) the end of solidification cracking at 0.832s of bending and an approximate strain of 10.53 % (adapted from [6])

Table 2: Summary of properties observed from in situ micro-radiography.

	EN1A			S303			Carbon		
	95mm/s	115mm/s	135mm/s	95mm/s	115mm/s	135mm/s	95mm/s	115mm/s	135mm/s
Crack initiation time (s)	0.15	0.11	0.13	0.52	0.26	0.22	0.19	0.16	0.18
Crack end time (s)	1.33	0.88	0.83	1.15	0.87	1.00	1.22	0.87	0.71
Cracking period (s)	1.19	0.77	0.70	0.63	0.61	0.78	1.03	0.71	0.52
Crack initiation strain	2.47	2.58	3.25	5.06	4.00	4.35	2.42	2.56	3.42
Cracking end strain	8.33	8.89	10.53	9.52	8.70	10.13	7.69	8.16	9.52
Cracking strain range	5.86	6.31	7.27	4.46	4.70	5.78	5.27	5.60	6.11
Crack nucleation depth (mm)	1.18	1.63	1.45	0.47	0.86	0.98	0.82	1.05	1.73
Fracture velocity (mm/s)	1.66	2.46	2.20	2.48	2.54	2.53	2.33	2.18	2.59

3.3. Mechanisms proposed for cracking during welding of low-alloy high-impurity steels

Figure 5 schematic the proposed formation mechanism of hot cracking during weld pool solidification. After the transition from the dendrite to the grain structure when the volume fraction of liquid is <0.1 and temperature is ~1430 °C, solute elements (Mn, Si, Al) and impurities (S) segregate to grain boundaries. As a result, low melting point films with eutectic chemistries form in the inter-granular regions. Under tensile strains of ~3.25%, hot cracks form sub-surface at the inter-granular sites where the eutectic liquid films are concentrated, as illustrated in Figure 5(a). The cavities initially form sub-surface in the weld centre, as illustrated in Figure 5(a) by the red globules.

As the loading increases, the hot cracks then coalesce, predominantly in the “y” direction through the fracture of network separating bridges. Sometimes the hot cracks remain isolated and sometimes they coalesce with each other but not the bulk crack, as evidenced in which circle in Figure 5(b). Eventually, it is proposed that the coalescence of the hot cracks propagates through the grain structure to the solidifying dendritic structure.

Once the coalescence of the inter-granular hot cracks has propagated through to the solidifying dendrite structure, hot tearing begins. At this stage, the volume fraction of liquid is higher and inter-dendritic fracture is observed from the separation of primary dendrite arms as a result of tensile deformation as described in Figure 5(c). As the propagation is linked to the solidifying dendrites, the propagation path is related to that of the growing dendrites in terms of direction (towards the heat source) and velocity (~2.2-2.8 mm/s. However, as the load is applied along the length of the weld (z-axis), the tearing of the dendrites is also induced parallel to the x-axis, resulting in the somewhat angular cracking path towards the heat source as illustrated in Figure 5(c) and evidenced in Figure 2.

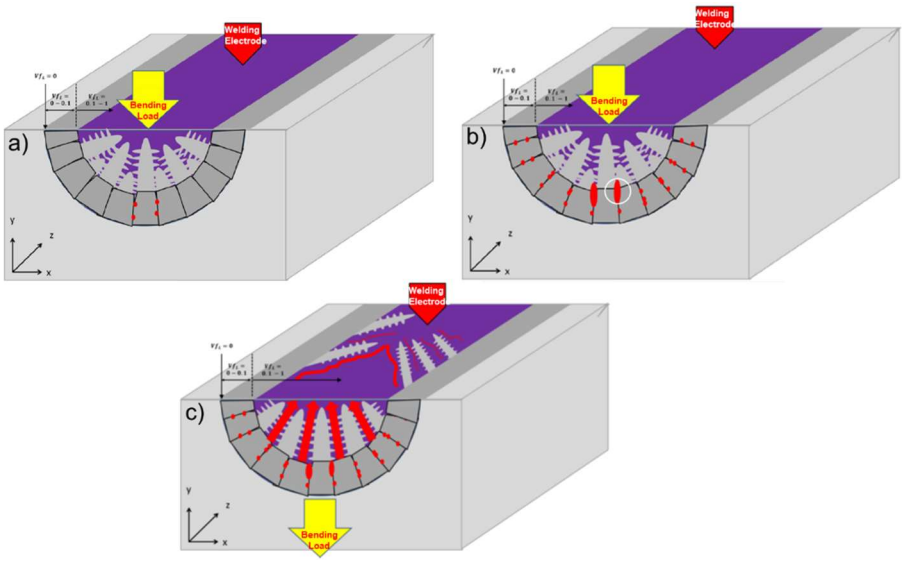

Figure 5: 3D schematic of hot crack formation mechanism in respect to weld pool: (a) inter-granular hot crack initiation; (b) coalescence of hot cracks; (c) hot tearing propagation.

Concluding Remarks

Weld solidification cracking in steel has been successfully observed *in situ* using a high speed, high energy, synchrotron X-ray radiography approach. Analysis of the *in situ* radiography sequence revealed the solidification cracking initiates in the weld sub-surface trailing the welding electrode. The results reveal that both material type and bending speed influence solidification cracking. However, the measured fracture velocity remains fairly consistent throughout the experiments with an average velocity of 2.33 mm/s calculated. In addition, a three-stage mechanistic model for solidification cracking during welding of steel is proposed.

References

[1] V. Shankar, J. Devletian, Science and Technology of Welding and Joining, 10 (2005) 236-243.
[2] S. Park, Ohio State University, 1989.
[3] J.R. Davis, Corrosion of Weldments, ASM International, Materials Park, OH, USA, 2006.
[4] I. Medovar, Avtomatich. , 7 (1954) 12–28.
[5] Aucott, L., Huang, D., Dong, H.B. et al. Metall and Mat Trans A (2018) 49: 1674.
[6] L. Aucott, D. Huang, H. B. Dong, S. W. Wen, J. A. Marsden, A. Rack & A. C. F. Cocks Scientific Reports (2017) volume 7, Article number: 40255
[7] I. Farup, J.M. Drezet, M. Rappaz, Acta Materialia, 49 (2001) 1261-1269.
[8] C.M. Gourlay, A.K. Dahle, T. Nagira, N. Nakatsuka, K. Nogita, K. Uesugi, H. Yasuda, Acta Materialia, 59 (2011) 4933-4943.
[9] S. Vernède, J.A. Dantzig, M. Rappaz, Acta Materialia, 57 (2009) 1554-1569.
[10] S. Vernède, M. Rappaz, Acta Materialia, 55 (2007) 1703-1710.
[11] S. Vernède, P. Jarry, M. Rappaz, Acta Materialia, 54 (2006) 4023-4034.
[12] A.B. Phillion, S.L. Cockcroft, P.D. Lee, Materials Science and Engineering: A, 491 (2008) 237-247.
[13] J. Aveson, IOP Conference Series: Materials Science and Engineering, 2012.
[14] K.M. Kareh, P.D. Lee, R.C. Atwood, T. Connolley, C.M. Gourlay, Nat Commun, 5 (2014).
[15] T. Weitkamp, P. Tafforeau, E. Boller, P. Cloetens, J.-P. Valade, P. Bernard, F.c.o. Peyrin, W. Ludwig, L. Helfen, J.e. Baruchel, AIP Conf. Proc. (ICXOM20), 1221 (2010) 35-38.